Intermolecular arrangement facilitated broadband blue emission in group-12 metal (Zn, Cd) hybrid halides and their applications

Dilruba A. Popy,[1] Brett N. Evans,[1] Jie Jiang,[2] Tielyr D. Creason,[1] Dhritiman Banerjee,[1] Lauren M. Loftus,[2,3] Ruth Pachter,[2] Daniel T. Glatzhofer,[1] Bayram Saparov[1*]

[1]*Department of Chemistry & Biochemistry, University of Oklahoma, Norman, OK, USA*

[2]*Materials and Manufacturing Directorate, Air Force Research Laboratory, Wright-Patterson Air Force Base, OH 45433, USA*

[3]*General Dynamics Information Technology, 5000 Springfield St. Suite 200, Dayton, OH 45431, USA*

*Author to whom correspondence should be addressed: saparov@ou.edu

ORCID ID: Dilruba A. Popy: 0000-0001-5017-3274; Tielyr D. Creason: 0000-0003-1688-8115; Lauren M. Loftus: 0000-0001-6829-3039; Ruth Pachter: 0000-0003-3790-4153; Bayram Saparov: 0000-0003-0190-9585.

Abstract: Various fluorescent organic materials are widely known for their potential applications in light-emitting diodes, organic lasers, anti-counterfeiting and bio-imaging. However, poor emission efficiency and stability issues limit their usability. Here we report the syntheses, crystal and electronic structures, and optical characterizations of two new hybrid organic-inorganic group 12 halides, (P-xd)$ZnCl_4$ and (P-xd)$CdCl_4$ (where (P-xd) = *p*-xylylenediammonium). Single crystals of both compounds can be conveniently synthesized by solution chemistry methods from their low-cost, low toxicity and easily available precursors. (P-xd)$ZnCl_4$ possesses a crystal structure featuring alternating layers of organic cations and completely separated anionic $[ZnCl_4]^{2-}$ tetrahedral units of zero-dimensional (0D) connectivity. In contrast, (P-xd)$CdCl_4$ adopts similar layering of organic cations sandwiched between perovskite sheets of two-dimensional (2D) connectivity, which are formed by corner-sharing anionic $[CdCl_6]^{4-}$ octahedral units. The structural, optical, and electronic studies suggest that the incorporation of organic and inorganic structural units into a hybrid structure improves its blue emission efficiency with nearly 23 times and 4 times higher photoluminescence quantum yield (PLQY) values in (P-xd)$ZnCl_4$ and (P-xd)$CdCl_4$, respectively, as compared to the organic precursor. Notably, PLQY of 23% for (P-xd)$ZnCl_4$ is the highest reported to date for Zn-based hybrid organic-inorganic metal halides, where emission originates from the organic component. Both (P-xd)$ZnCl_4$ and (P-xd)$CdCl_4$ demonstrate considerably improved air-, thermal- and photostability, which suggest their suitability for potential practical applications such as fingerprint detection and solid-state lighting.

Keywords: Group 12 hybrid metal halides, intermolecular arrangements, quantum confinement effect, photostability, optical applications.

1. Introduction

The structural versatility and tunability of organic fluorescent materials have attracted the attention of researchers over the decades for their intended uses in solid-state lasers, light-emitting diodes (LEDs), sensors, anticounterfeiting and bio-imaging applications.[1-4] The photoluminescence (PL) efficiency of pure organic molecules is generally weak because of the concentration quenching effect and nonradiative recombination of excitons influenced by the structural arrangements, aggregation, stacking patterns, etc.[5-10] Therefore, many strategies have been developed to improve the optical properties of organic molecules by structural modifications including functional group introductions, polymer matrix embedding, and metal-organic framework constructions.[11-15] However, the suitability of these methods is limited due to the multi-step synthesis methods and involvement of complex molecular structures. Notwithstanding these challenges, further development of this field is of great importance to achieve the desired photophysical properties of emissive organic centers for practical applications.

Separately, solution-processable hybrid organic-inorganic metal halides (HOIMs) have also attracted much attention in the past decade because of their low cost, ease of synthesis via a variety of methods, tunable structural dimensionality and broadly tunable photophysical properties.[16-19] The crystal structure dimensionality, which refers to the connectivity of the inorganic part of the structure in this field, can be manipulated by varying organic, metal and halogen sites in pseudo-ternary A – B – X (A = organic cation, B = metal cation, X = halide anion) HOIMs.[20] Importantly, the control over chemical compositions and structural dimensionality of HOIMs provides an avenue for an unprecedented control over photophysical properties of these hybrid materials. Thus, it was demonstrated that progressive lowering of the structural dimensionality of HOIMs results in increasing charge localization and higher exciton binding energies.[16,21] Highest charge localizations are often observed in compounds possessing zero-dimensional (0D) connectivity of structural units in which quantum confinement effect is maximized, thereby facilitating the formation of stable excitons at room temperature, and providing enhanced excitonic emission.[17]

In addition to the structural dimensionality changes, the desired experimental control over photophysical properties of HOIMs can also be achieved by incorporating photoactive A^{n+} organic cations into A – B – X hybrids. Pursuing this idea, many hybrid organic-inorganic materials containing photo-active organic components have been explored in recent years. Typically, the resultant photoemission properties of high-efficiency light emitting HOIMs mainly originate from the inorganic structural units, or the synergistic contributions of both organic and inorganic units.[22-25] In comparison, less attention is devoted to the optimization of light emission originating from the organic components in HOIMs; in principle, periodical embedding of photoluminescent organic molecules into an inorganic structural framework can also produce high-efficiency light emitters for target practical applications. Recent studies on Pb-, Bi- and Sn-based hybrid halide perovskites featuring quinoline derivatives report significant improvements of light emission efficiency in HOIMs (as compared to the precursor organics), supporting the validity of this idea.[26-28] Further extending this strategy, if the photoactive unit in

the structure is the organic part, one can explore earth-abundant, low-cost, and environmentally stable metal halides as guest materials, e.g., instead of the undesirable, toxic and heavy metal Pb-based halides.

In this context, group 12 metals have attracted great attention due to their low cost, earth-abundance and low toxicity (e.g., Zn), and low electronegativity (e.g., Zn, Cd); the latter is particularly important as it indicates that Zn and Cd halides are likely to have wide inorganic bandgaps due to their large metal-halogen electronegativity differences.[21,22,29-35] Advantageously, unlike high electronegativity metals such as Bi, Sn and Pb, the large bandgaps of [(Zn, Cd)-X] inorganic frameworks lead to mostly optically inactive metal halide centers in the visible range, allowing for a targeted visible emission from the organic cations. However, although the incorporation of zinc and cadmium halides in organic lattice have been reported to improve the emission efficiency of organic photoactive components, photoluminescence quantum yield (PLQY) values of the literature reported Zn- and Cd-based HOIMs are typically low (<20%).[22,30] In the few Zn-based hybrid materials with PLQYs higher than 20% (e.g., 42.5% in $(C_9H_{15}N_3)ZnCl_4$, 35.47% in (EP)$ZnBr_4$ (EP = 1-ethylpiperazine) and 24.58% in (BP)$ZnBr_4$ (1-phenylpiperazine)), inorganic structural units or the synergetic effects of both organic and inorganic structural units contribute to their light emission properties.[33,34] The light emission contribution from both organic and inorganic components may lead to unpredictability of PL properties of Zn-based HOIMs as major changes occur in PL as compared to the expected emission solely from the organic structural components.

In this work, we report two new Zn- and Cd-based HOIMs (P-xd)$ZnCl_4$ and (P-xd)$CdCl_4$, containing *p*-xylylenediammonium (P-xd) as the organic component. Xylylenediamine and its derivatives can act as structurally flexible chromophore due to the presence of two electron donating amine centers, yet their optical properties are widely unexplored. Here, the introduction of Zn and Cd halides polyhedral units into the *p*-xylylenediammonium lattice leads to the formation of 0D and 2D-connectivity of inorganic structural units in (P-xd)$ZnCl_4$ and (P-xd)$CdCl_4$, respectively. Both compounds exhibit wide optical bandgaps of ~4.36 eV. While the organic precursor salt is a weak blue emitter, (P-xd)$ZnCl_4$ and (P-xd)$CdCl_4$ display bright blue emission with nearly 23 and 4 fold improved PLQY values, respectively. The structural analysis and experimental results of both compounds are discussed in conjunction with theoretical results to reveal the underlying mechanism of the emission properties of these compounds. The much-improved air, thermal and photostability of the novel compounds allow their consideration for potential practical applications, which is demonstrated through their use in fingerprint detection and solid-state lighting.

2. Experimental Section

2.1. Materials

Zinc(II) chloride (98+%, Alfa Aesar), cadmium(II) chloride (≥99%, Acros Organics), *p*-xylylenediamine (>99%, Tokyo Chemical Industry), and hydrochloric acid (36%, Alfa Aesar) were purchased and used as received with no further purification. All synthetic procedures were carried out in ambient air in a fume hood unless otherwise stated.

2.2. (P-xd)Cl_2 (p-xylylenediammonium chloride) synthesis

A 1.00 g (7.00 mmol) amount of *p*-xylylenediamine was dissolved in 10 ml of deionized water in a beaker followed by the addition of 1.2 mL (14.00 mmol) of 12M hydrochloric acid. The solvent was slowly evaporated at room temperature. The colorless crystalline solids of (P-xd)Cl_2 were collected and dried under vacuum. The purity of the product was ensured from the similarity of the powder x-ray diffraction (PXRD) data of the product with the reported data.[36] The product was stored at room temperature and ambient conditions.

2.3. (P-xd)$ZnCl_4$ synthesis

(P-xd)Cl_2 (209 mg, 1.00 mmol) and $ZnCl_2$ (136 mg, 1.00 mmol) were dissolved separately in 3 mL deionized water at room temperature after which solutions were mixed together to get a clear precursor solution. The precursor solution was evaporated at 50 ℃ for 4 hours and then allowed to cool to room temperature. The colorless needle shaped crystals of (P-xd)$ZnCl_4$ were collected and dried under vacuum and stored in ambient conditions for further characterization.

2.4. (P-xd)$CdCl_4$ synthesis

(P-xd)Cl_2 (209 mg, 1.00 mmol) and $CdCl_2$ (183 mg, 1.00 mmol) were dissolved separately in 3 mL deionized water at room temperature; mixing of these solutions yielded a clear precursor solution. The precursor solution was evaporated at 50 ℃ for 4 hours and then allowed to cool to room temperature. The colorless flat crystals of (P-xd)$CdCl_4$ were collected and dried under vacuum and stored in ambient conditions for further characterization.

2.5. Preparation of luminescent inks using (P-xd)MCl_4 (M = Zn, Cd)

Two grams of polymethylmethacrylate (PMMA) were added to 6 ml of toluene and stirred at room temperature until PMMA was completely dissolved. Solution-grown single crystals of the title compounds were ground into a polycrystalline powder sample, from which 300 mg was used for the ink preparation; powder sample was dispersed into the PMMA solution by stirring for one day. This luminescent ink was used for printing latent fingerprints, graffiti, and coating a 365 nm commercial UV LED chip to fabricate blue light-emitting diodes.

2.6. Powder X-ray Diffraction (PXRD) measurements

Powder X-ray diffraction (PXRD) measurements were carried out at room temperature using a Rigaku MiniFlex600 system equipped with a Ni-filtered Cu Kα radiation source. PXRD scans were performed on polycrystalline samples in the 3 – 90° (2θ) range with a step of 0.02°, and the XRD patterns were analyzed using a PDXL2 software package. Obtained PXRD patterns were fit using the decomposition method. To test the air-stability of (P-xd)MX_4 (M = Zn, Cd), powder samples were left on a laboratory bench under ambient air conditions (20 °C and 30% relative humidity) for four months, during which periodic PXRD measurements were performed.

2.7. Single Crystal X-ray Diffraction (SCXRD) measurements

Single crystal X-ray diffraction (SCXRD) measurements were performed using a Bruker D8 Quest Kappa-geometry diffractometer with an Incoatec Iμs microfocus Mo Kα X-ray source and a Photon II area detector. The data were corrected for absorption using the semiempirical method based on equivalent reflections, and crystal structures were solved by intrinsic phasing methods as embedded in the APEX3 v2015.5-2 program. Site occupancy factors were checked by freeing occupancies of each unique crystallographic positions. Details of the data collection and

crystallographic parameters are given in Table S1. Atomic coordinates, equivalent isotropic displacement parameters, and selected interatomic distances, and bond angles are provided in Tables S2-S4. The Crystallographic Information Files (CIFs) were deposited in the Cambridge Crystallographic Data Centre (CCDC) database (deposition numbers 2221549 – 2221550).

2.8. Thermogravimetric Analysis and Differential Scanning Calorimetry (TGA/DSC) measurements

Simultaneous thermogravimetric analysis and differential scanning calorimetry (TGA/DSC) were measured on ~10 mg samples of the title compounds on a TA Instruments SDT 650 thermal analyzer system. Crystals were heated up from 25 °C to 475 °C under an inert nitrogen gas flow at a rate of 100 mL/min, with a heating rate of 5 °C/min.

2.9. Photoluminescence measurements

Room-temperature photoluminescence (PL) emission and photoluminescence excitation (PLE) measurements were carried out on single crystal samples of the respective title compounds using HORIBA Jobin Yvon Fluorolog-3 spectrofluorometer with Xenon lamp source and Quanta-Φ integrating sphere. Data were collected using the two-curve method in a varied range from 250 to 750 nm. The Commission Internationale de l'Eclairage (CIE) color plots were generated using a GoCIE software. For the photostability measurement, the polycrystalline sample of the respective title compound was placed inside the Quanta-φ integrating sphere on the Jobin Yvon Fluorolog-3 spectrofluorometer. The sample was then exposed to the full power of the Xenon lamp at its PL excitation maximum wavelength. Periodic PLQY measurements were taken every 5 min under these conditions for a total of 60 minutes.

Photoluminescence lifetimes were collected at room temperature using an Edinburgh Instruments FLS980 spectrometer using time-correlated single photon counting (TCSPC) at the indicated emission wavelengths. The samples were loaded into a 1 mm pathlength quartz cuvette that was placed at a 45° angle relative to the excitation source, and they were excited using an EPLED-320 pulsed LED diode (Edinburgh Instruments, center wavelength = 313.8 ± 10 nm, pulse width = 0.9498 ns). The emission signal was collected at 90° relative to the excitation source and passed through a Czerny-Turner monochromator (300 nm focal length, 1800 grooves/mm grating, 1.8 nm/mm linear dispersion) prior to being collected with a Hamamatsu R928P side window photomultiplier tube in a cooled housing (operating temperature: -20 ℃). A 350 nm longpass filter was placed between the sample and the monochromator to filter out scattered light from the excitation source. Reconvolution fits of the photoluminescence decays and the instrument response function (IRF) were performed using the Edinburgh Instruments F900 software package; the fits for each compound are shown in Fig. S10, and the lifetime results are compiled in Table S5.

2.10. Diffuse reflectance measurements

UV-vis diffuse reflectance data were collected on powder samples of the title compounds using a PerkinElmer Lambda 750 UV-vis-NIR spectrometer with a 100 mm Spectralon InGaAs Integrating Sphere over a range of 250-1100 nm. Diffuse reflectance data were then transformed

to pseudo-absorption spectra utilizing the Kubelka-Munk function $F(R) = {}^{\alpha}/_{S} = {}^{(1-R)^2}/_{2R}$, where α is the absorption coefficient, S is the scattering coefficient, and R is the reflectance.

2.11. Density Functional Theory (DFT) Calculations

DFT calculations were performed with the Vienna ab initio simulation package (VASP 5.4),[37,38] applying the projector augmented-wave (PAW) potential. The Kohn-Sham equations were solved using a plane wave basis set with an energy cutoff of 500 eV. A 3×2×3 *k*-point sampling was used for the primitive cell of the (P-xd)$ZnCl_4$ structure and 3×4×4 *k*-point sampling for the (P-xd)$CdCl_4$ structure. The experimentally determined crystal structures were optimized using the Perdew-Burke-Ernzerhof (PBE) exchange-correlation functional,[39] including the zero damping D3 correction of Grimme,[40] as inclusion of London dispersion is important in modeling the π–stacking demonstrated for (P-xd)$ZnCl_4$ and (P-xd)$CdCl_4$, previously emphasized for treating halide perovskites,[41] and has been applied.[42] Geometries were fully relaxed regarding lattice parameters and interatomic distances until forces were less than 0.01 eV/Å. The Heyd-Scuseria-Ernzerhof (HSE06) range-separated functional was employed for band structure calculations.[43,44]

3. Results and Discussion

3.1. Structure, stability, optical and electronic properties

(P-xd)$ZnCl_4$ and (P-xd)$CdCl_4$ can be grown as flat needle and thin plate crystals (Fig. 1), respectively, using a simple, low-cost water solution synthesis method. A schematic representation of the employed synthetic method is shown in Scheme 1 (see section 2.3 and 2.4 for more details). The easy accessibility of optoelectronic metal halides through simple solution processing is one of their advantageous characteristics. The phase purity and crystallinity of the as-synthesized products were ensured by PXRD measurements at room temperature (Fig. 1c and d). The crystals of (P-xd)$ZnCl_4$ and (P-xd)$CdCl_4$ are colorless under ambient light and emit blue light under UV irradiation (Fig. S1).

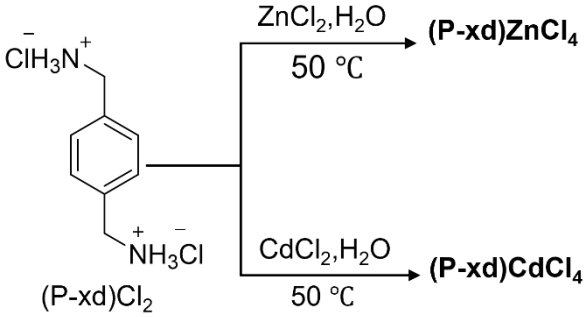

Scheme. 1 Schematic representation of the synthesis process of (P-xd)$ZnCl_4$ and (P-xd)$CdCl_4$ from (P-xd)Cl_2.

The results of SCXRD experiments for (P-xd)$ZnCl_4$ and (P-xd)$CdCl_4$ are summarized in Tables S1-S4. Although (P-xd)$ZnCl_4$ and (P-xd)$CdCl_4$ are not isostructural, both crystallize in the monoclinic crystal system within the centrosymmetric space group $P2_1/c$. (P-xd)$ZnCl_4$ adopts a crystal structure built upon inorganic anionic $[ZnCl_4]^{2-}$ tetrahedra completely separated from

each other (0D-connectivity) by the organic cationic $(P\text{-}xd)^{2+}$ units (Figs. 1e and S2a). Notably, the anionic $[ZnCl_4]^{2-}$ tetrahedra extend along the *bc*-plane, alternating with layers of the cationic $(P\text{-}xd)^{2+}$ units along the *a*-axis, resulting in a pseudo-layered crystal structure. Such type of pseudo-layered packing structure of alternating inorganic and organic units is a common feature for many low dimensional hybrid metal halides including other group 12 metal halides.[22,30,31,34] In the 0D-connectivity of $(P\text{-}xd)ZnCl_4$, Zn^{2+} is coordinated with four Cl^- in slightly distorted tetrahedral environment; $[ZnCl_4]^{2-}$ tetrahedra feature Zn-Cl bond lengths and Cl-Zn-Cl bond angles ranging from 2.26136(6) Å to 2.2828(7) Å and 110.78(3)º to 115.21(3)º, respectively (see Fig. S4a). The polyhedral distortions in metal halides are most typically attributed to the presence of stereoactive lone pairs on metal centers (e.g., in lead halide perovskites), however, since Zn^{2+} has a $3d^{10}$ electronic configuration, the distortion in the present case is most likely due to the optimized packing of organic and inorganic molecular anions. This agrees with the observations made for 0D hybrid zinc halides where the presence of distortion in $[ZnCl_4]^{2-}$ is related to the arrangements of organic cations in the adjacent organic layers.[22,30,33-35] Interestingly, the inorganic and organic units are stacked in two different rotational positions, allowing the organic units to maintain the shortest distance of their protonated end towards the nearby anionic sites, where the rotational direction repeats in every other layer (see Fig. S2a). These types of rotational packings also help to avoid the steric hinderance among the adjacent structural units. Moreover, because of such packing, the shortest intermolecular Cl--Cl distance of 3.826 Å is observed between the adjacent $[ZnCl_4]^{2-}$ tetrahedra, which is more than twice longer than the Shannon ionic radius of chloride ion ($2 \times r(Cl^-) = 3.62$ Å) (see Fig. S5a).[45] Such large distances between neighboring tetrahedral inorganic anions is indicative of minimal electronic coupling between the inorganic tetrahedral anions, which is typical for 0D structures with increased charge localization and quantum confinement. Notably, the pure $(P\text{-}xd)Cl_2$ crystal structure also possesses pseudo-layered arrangements of $(P\text{-}xd)^{2+}$ organic cations, however, all of the cations are packed in the same orientation (see Fig. S3).[36]

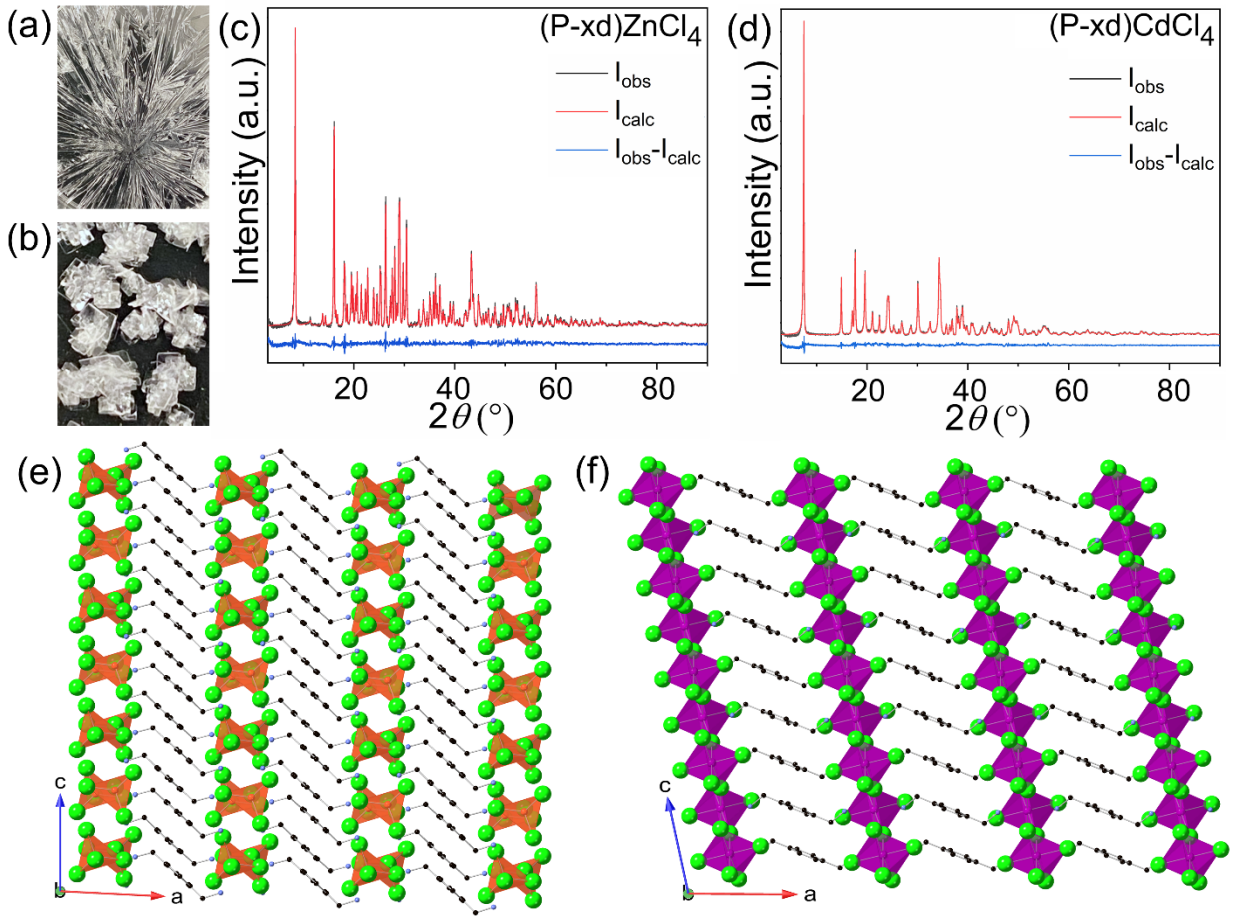

Fig. 1 Photographs of the single crystals of (a) (P-xd)$ZnCl_4$ and (b) (P-xd)$CdCl_4$. Room-temperature PXRD patterns (in black) fitted using the Pawley method (in red) for (c) (P-xd)$ZnCl_4$ and (d) (P-xd)$CdCl_4$. Difference between the measured and calculated patterns are shown in blue. Polyhedral representations of the crystal structures of (e) (P-xd)$ZnCl_4$ and (f) (P-xd)$CdCl_4$ along the *b*-axis. Orange, violet, green, blue, and black spheres represent zinc, cadmium, chlorine, nitrogen, and carbon, respectively. For clarity, H atoms are not depicted.

In comparison, (P-xd)$CdCl_4$ adopts a 2D layered perovskite structure with alternating layers of organic cations and n = 1 inorganic $[CdCl_4]^{2-}$ sheets made of vertex connected $[CdCl_6]^{4-}$ octahedra; the organic cationic $(P\text{-}xd)^{2+}$ layer is similar to that of (P-xd)$ZnCl_4$ structure (Fig. 1f and S2b). The markedly different structures of (P-xd)$ZnCl_4$ and (f) (P-xd)$CdCl_4$ can be explained using Pauling's Radius Ratio Rules. Thus, based on the ratios of metal cation (r_M) and chloride anion (r_{Cl}) Shannon radii,[45] $\mu = r_M/r_{Cl}$, an octahedral coordination environment is preferred by Cd(II) in chlorides (μ_{oct} = 0.525), whereas the octahedral factor of μ_{oct} = 0.409 calculated for Zn(II) in chlorides is below the acceptable range of 0.414–0.732 for an octahedral structure. Given the 2D connectivity of the $[CdCl_6]^{4-}$ octahedra in (P-xd)$CdCl_4$, this compound is expected to have reduced quantum confinement compared to the 0D compound (P-xd)$ZnCl_4$.[16,21] The structure of (P-xd)$CdCl_4$ possesses two different rotational positions of $[CdCl_6]^{4-}$ anions and $(P\text{-}xd)^{2+}$ cations while layering along *c*-axis (see Fig. S2). Interestingly, cadmium halide octahedra can be highly distorted such as in the case of $(C_6H_{11}NH_3)_2CdBr_4$, in which the $[CdBr_4]^{2-}$ perovskite layer is formed by very distorted $[CdBr_6]^{4-}$ octahedra featuring 4 close and 2

elongated bonds.[32] This has been attributed to the templating influence of the organic cation via hydrogen bonding interactions. In the case of (P-xd)$CdCl_4$, the Cd-Cl bond distances in $[CdCl_6]^{4-}$ anions range from 2.55 Å to 2.67 Å.[46] Fig. S4 shows the coordination environments around metal centers in (P-xd)$ZnCl_4$ and (P-xd)$CdCl_4$, including select metal halide bond lengths and bond angles. The bridging chlorines of the octahedral layer have bond distances of 2.67 Å (Cd1-Cl1) while the singly bound chlorines have a bond distance of 2.55 Å (Cd1-Cl2). The bridging chlorine also displayed the highest distortion angle of 159.3° (Cd1-Cl1-Cd1), while the highest distorted bond angle within the octahedron is 87.410° (Cl1-Cd1-Cl2). This creates a wave-like pattern within the perovskite layer. The long Cl--Cl interlayer distances (>7.396 Å) suggests negligible interactions between the adjacent inorganic sheets in (P-xd)$CdCl_4$ (Fig. S5b).

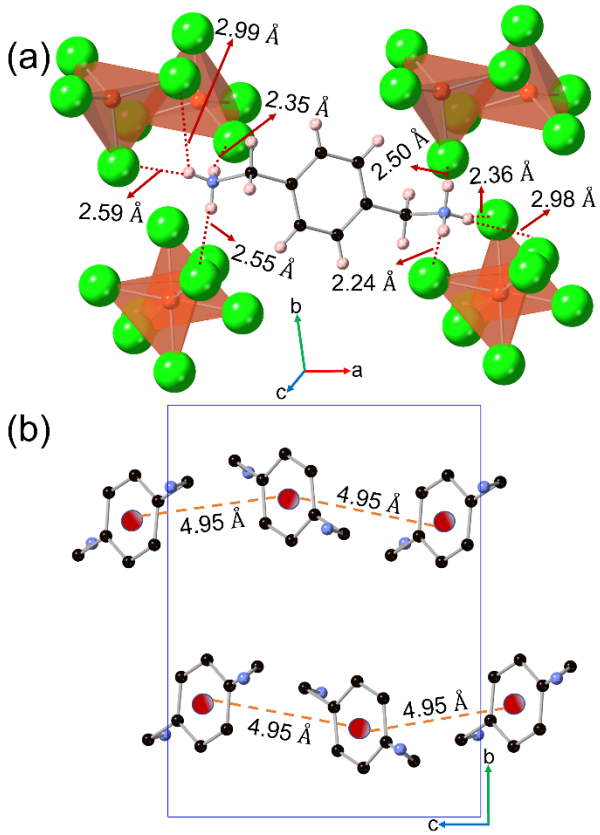

Fig. 2 (a) Hydrogen bonding contacts in (P-xd)$ZnCl_4$. (b) Intermolecular distances in the cationic $(P\text{-xd})^{2+}$ layer in (P-xd)$ZnCl_4$ (red sphere represents imaginary central atom; coloring of atoms is identical to that in Fig. 1).

The pseudo-layered structures of both (P-xd)$ZnCl_4$ and (P-xd)$CdCl_4$ exhibit H-bonding interactions from both nitrogen positions of $(P\text{-xd})^{2+}$. Here we will discuss the situation for (P-xd)$ZnCl_4$ in detail as a representative compound. In (P-xd)$ZnCl_4$, all three H atoms attached to N-atom maintain Cl··H distances ranging from 2.24 Å to 2.59 Å (Fig. 2a), suggesting moderately strong H-bonding interactions.[47] These H-bonding distances are aligned very well with other similarly organized pseudo-layered hybrid zinc halide systems.[22,30,48] The H-bonding interaction in (P-xd)$ZnCl_4$ is slightly stronger than that of the pure (P-xd)Cl_2 organic salt where the shortest Cl··H distance is 2.28 Å (Fig. S6a). Moreover, the presence of H-bonding in both N-atom sites

keeps the $(P\text{-}xd)^{2+}$ organic units in highly ordered arrangements and makes the structure of $(P\text{-}xd)ZnCl_4$ very stable. Similar types of H-bonding are also present in $(P\text{-}xd)CdCl_4$ with Cl··H distances ranging from 2.32 Å to 2.50 Å. In addition to the H-bonding interactions, π–stacking interactions of neighboring $(P\text{-}xd)^{2+}$ units also contribute towards the structural stability and rigidity of $(P\text{-}xd)ZnCl_4$ and $(P\text{-}xd)CdCl_4$. Due to the presence of different rotational positions of $(P\text{-}xd)^{2+}$ units as discussed above, two neighboring aromatic rings maintain 4.95 Å distances throughout the bilayer structure in $(P\text{-}xd)ZnCl_4$ (Fig. 2b). In comparison, this distance in the precursor organic salt $(P\text{-}xd)Cl_2$ is 4.35 Å (see Fig. S6b). To summarize, the inclusion of inorganic polyhedral units in the organic $(P\text{-}xd)^{2+}$ lattice to obtain $(P\text{-}xd)ZnCl_4$ and $(P\text{-}xd)CdCl_4$, leads to the alternating packing of organic and inorganic units in their structures and changes in H-bonding interactions, and consequently, results in increased structural rigidity and effective suppression of the aggregation of organic units. The latter is important for the optical properties of resultant hybrids as aggregation of organic molecular units is a known cause of quenched PL in organics.

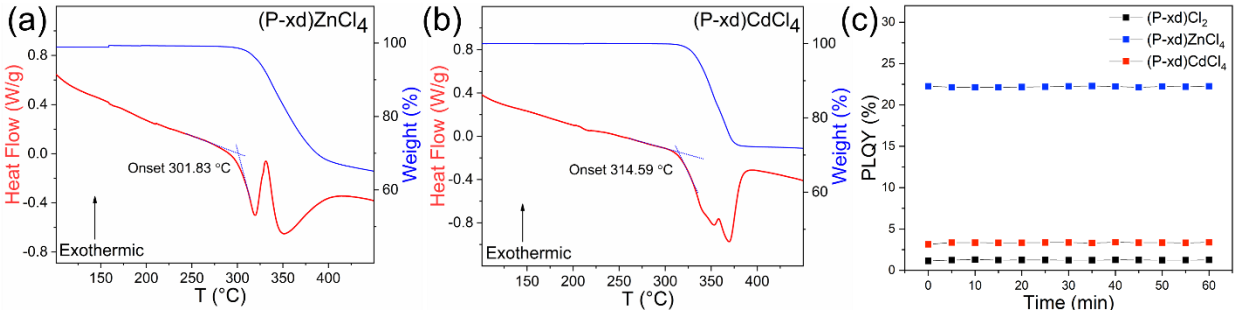

Fig. 3 Thermogravimetric analysis (TGA) and differential scanning calorimetry (DSC) measurement results for (a) $(P\text{-}xd)ZnCl_4$ and (b) $(P\text{-}xd)CdCl_4$. (c) Normalized photoluminescence quantum yield (PLQY) under continuous irradiation over 60 minutes at PLE_{max} for $(P\text{-}xd)Cl_2$, $(P\text{-}xd)ZnCl_4$ and $(P\text{-}xd)CdCl_4$.

To determine the ambient air stability of the as synthesized samples, periodic PXRD measurements of $(P\text{-}xd)ZnCl_4$ and $(P\text{-}xd)CdCl_4$ were carried out under ambient conditions (i.e., 20 ˚C and relative humidity of 30%) over a period of 4-months. The results suggest that $(P\text{-}xd)ZnCl_4$ and $(P\text{-}xd)CdCl_4$ are stable in air for months (Fig. S7). Moreover, both $(P\text{-}xd)ZnCl_4$ and $(P\text{-}xd)CdCl_4$ showed improved thermal stability with no significant loss of weight up to 300 ˚C based on thermogravimetric analysis (TGA) (Fig. 3). The differential scanning calorimetry (DSC) results for both compounds are in good agreement with the melting point measurement experiments. The TGA/DSC results suggest that both compounds decompose above 300 ˚C. The first decomposition events starting at ~300 ˚C for both compounds are characterized by the release of white fumes (observed during MP measurements). The corresponding weight loss percentages of 32% and 28% of $(P\text{-}xd)ZnCl_4$ and $(P\text{-}xd)CdCl_4$, respectively, and releases of white fumes suggest the release of two molecules of NH_4Cl from each compound. This event is followed by a second transition near 350 ˚C where melting transitions of the remaining sample occurs. The TGA/DSC results of pure organic salt, $(P\text{-}xd)Cl_2$, also demonstrated the occurrence of a thermal event starting at ~300 ˚C accompanied by 85% weight loss (Fig. S8). These results

suggest improved air and thermal stability of both hybrid compounds reported in this work compared to the previously reported group 12 metal halides such as R_2MCl_4 (M = Zn, Cd; R = $C_{13}H_{12}N$), $(4AMP)_2ZnBr_4$ (4AMP = 4-aminopyridinium), $(4AMP)_2HgBr_4 \cdot H_2O$, $(R)ZnBr_3(DMSO)$, $(R)_2CdBr_4 \cdot DMSO$, and $(R)CdI_3(DMSO)$ ((R) = $C_6(CH_3)_5CH_2N(CH_3)_3$, and DMSO = dimethyl sulfoxide), and $(H_2TTz)ZnX_4 \cdot MeOH$ (TTz = 2,5-bis(4-pyridinium)thiazolo[5,4-d]thiazole, and X = Cl, Br).[22,31,35,49] Finally, the photostability of (P-xd)$ZnCl_4$ and (P-xd)$CdCl_4$ were also measured by irradiating the as-synthesized materials with their corresponding excitation maxima for over 60 minutes. The optical properties of both (P-xd)$ZnCl_4$ and (P-xd)$CdCl_4$ remained unchanged after 60 minutes of UV exposure (Fig. 3c), which indicates high photostability of these materials in addition to their air and thermal stability properties. Altogether, the improved stability of (P-xd)$ZnCl_4$ and (P-xd)$CdCl_4$ make them potential candidates for optical applications.

Fig. 4 shows the UV-vis optical absorption and photoluminescence excitation (PLE) and emission (PL) spectra of (P-xd)Cl_2, (P-xd)$ZnCl_4$ and (P-xd)$CdCl_4$. (P-xd)Cl_2 is a colorless salt that emits weak blue light under UV irradiation (Fig. 4a). The broadband PL spectrum with a maximum at 436 nm and vibronic features at 415 nm and 465 nm was recorded for (P-xd)Cl_2 under 274 nm excitation, and is assigned as emission from the S_1 excited state of the organic cation that is most likely $\pi\pi^*$ in nature.[28,49] Single crystals of (P-xd)$ZnCl_4$ and (P-xd)$CdCl_4$ also show similar PL spectra but with significantly brighter blue emission and PL maxima at 443 nm and 435 nm under 285 nm and 287 nm excitation, respectively. Since both excitation and emission peak positions and shapes are largely similar, the photoemission at their corresponding excitation maxima for (P-xd)$ZnCl_4$ and (P-xd)$CdCl_4$ can be mainly attributed to the organic molecular units. To confirm the organic dominated photoluminescence of (P-xd)$ZnCl_4$ and (P-xd)$CdCl_4$, we performed in-depth optical spectroscopy and computational investigations, which are discussed next.

Immediately noticeable is the fact that the excitation and emission properties of the organic salt and (P-xd)$ZnCl_4$ are largely identical, except for the presence of a higher energy emission peak in the organic salt at 315 nm. The loss of this high energy shoulder peak in the hybrid compound (P-xd)$ZnCl_4$ may be due to different orientations and packing of the organic molecular units in (P-xd)$ZnCl_4$. In the specific case of (P-xd)$ZnCl_4$, the zinc chloride tetrahedra possess a wide bandgap and are not expected to demonstrate band-to-band transitions in the visible range.[35] However, below gap emission from $[ZnX_4]^{2-}$ tetrahedra, e.g., due to self-trapped excitonic (STE) emission, can contribute to the visible light emission of hybrid zinc halides.[22,33] In the present case, the spectral range of PL for (P-xd)$ZnCl_4$ largely is identical to that of the precursor organic salt, and no other additional contribution is immediately noticeable. Therefore, the broadband emission with peak maximum at 443 nm of (P-xd)$ZnCl_4$ can be attributed to emission from the S_1 excited state of the organic cation. Similarly, the emission of (P-xd)$CdCl_4$ with peak maximum at 435 nm can also be attributed to the organic structural units. Our attribution to the organic originated blue emission of both compounds in this paper is further supported by the similar values of the Commission Internationale de l'Eclairage (CIE) color coordinates of the organic salt and compounds (P-xd)$ZnCl_4$ and (P-xd)$CdCl_4$ at (0.14, 0.09), (0.14, 0.13) and (0.14, 0.14), respectively, obtained under UV irradiation at PLE_{max} of the corresponding compounds (see Fig. S9).

To further support the assignment of the observed luminescence to the organic molecular emission, PL lifetimes of all three compounds were collected using time-correlated single photon

counting (TCSPC). Excitation with 320 nm leads to similar PL behavior across the series, with the organic salt and both the Zn- and Cd-based hybrids exhibiting PL lifetimes of ~4 ns (Fig. S10) at 443 nm wavelength (see Table S5). This is in a good agreement with the fast emission originating from the organic component at this spectral region. Note that nanosecond-range short lifetimes attributed to fast singlet emission from organic molecules were also reported for several other Zn and Cd based hybrids (see Table S6).[22,35,49]

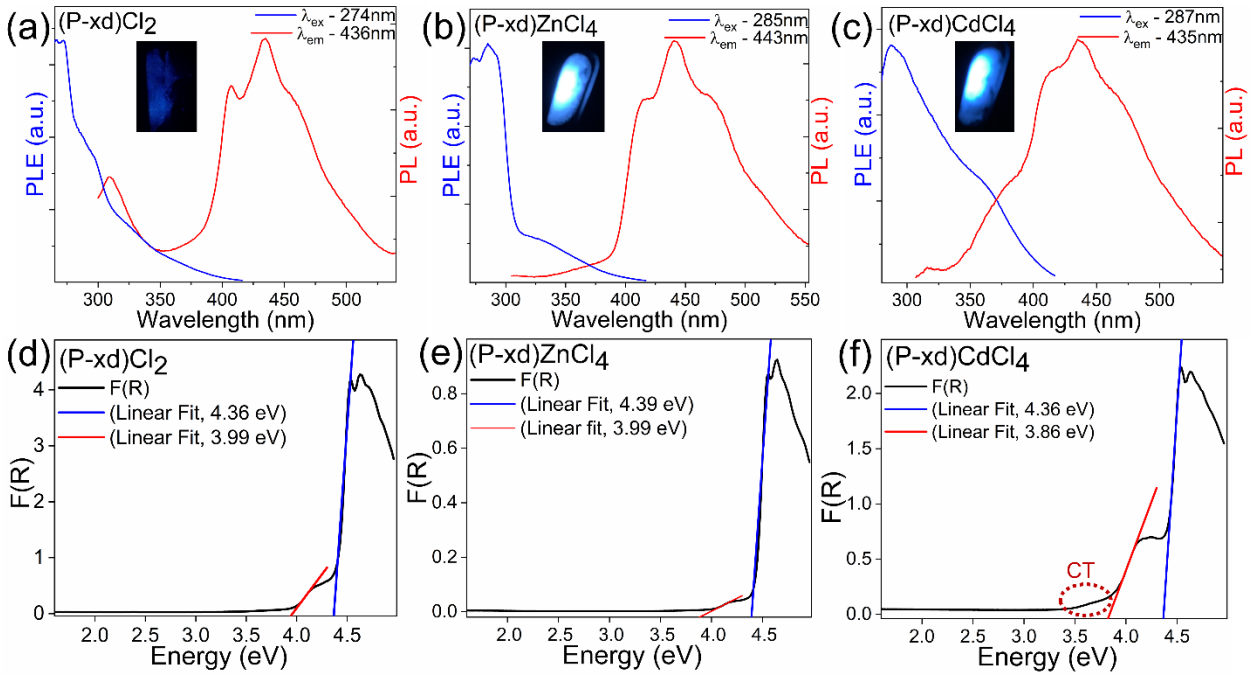

Fig. 4 Photoluminescence excitation (PLE) (blue) and photoluminescence emission (PL) (red) spectra at room temperature: (a) (P-xd)Cl_2, (b) (P-xd)$ZnCl_4$ and (c) (P-xd)$CdCl_4$. The insets show the light emission of the corresponding compound under excitation at PLE_{max}. Optical absorption data obtained using the Kubelka–Munk function, F(R), for (d) (P-xd)Cl_2, (e) (P-xd)$ZnCl_4$ and (f) (P-xd)$CdCl_4$. CT indicates the weak absorption corresponding to the charge transfer between the organic orbitals and inorganic bands.

To better understand the optical transitions in these compounds, optical absorption data were obtained using diffuse reflectance measurements (Fig. 4d – f). All three compounds are colorless, and unsurprisingly, they do not absorb in the visible region. The obtained absorption data for the organic salt, (P-xd)$ZnCl_4$ and (P-xd)$CdCl_4$ are largely similar. The nearly identical absorption spectra and similar onsets of absorption indicates that the states around the band gap have major contributions from the organic structural part in (P-xd)$ZnCl_4$ and (P-xd)$CdCl_4$. The high energy absorption bands above ~4 eV correspond to ππ* transitions within the $(P\text{-xd})^{2+}$ cations. The excitation maxima for both (P-xd)$ZnCl_4$ and (P-xd)$CdCl_4$ match with the onsets of sharp absorption peaks at 4.39 eV and 4.36 eV, respectively (see Fig. 4). These results support the assignment of photoemission to organic molecular emission in (P-xd)$ZnCl_4$ and (P-xd)$CdCl_4$. Despite the overall similarities, however, there are also noticeable differences below 4 eV. Unlike the pure organic salt and (P-xd)$ZnCl_4$, a weak absorption band with an onset of ~3.4 eV is present in the optical absorption spectrum of (P-xd)$CdCl_4$ (indicated by a red circle in Fig. 4f).

This weak absorption feature below 4 eV is attributed to a charge transfer from the organic orbitals to the inorganic bands (see the computational discussion below). Indeed, past work on low-dimensional hybrid metal halides has shown that such charge transfers between spatially separated structural parts lead to small optical matrix elements and weak absorption onsets. Furthermore, the presence of inorganic mid-gap states may contribute to the spatial separation of charge carriers in different structural units and may reduce the emission efficiency.[50]

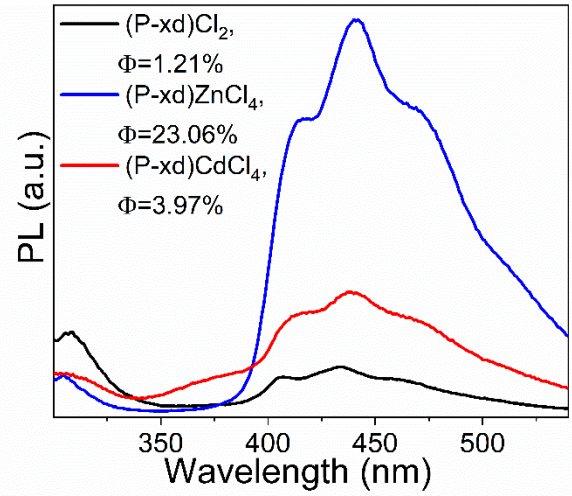

Fig. 5 Comparison of photoluminescence emission spectra for (P-xd)Cl_2, (P-xd)$ZnCl_4$ and (P-xd)$CdCl_4$.

The emission efficiency of the as-prepared materials was evaluated through photoluminescence quantum yield (PLQY) measurements carried out at their respective maximum excitation wavelengths (Fig. 5). The pure organic salt (P-xd)Cl_2 is measured to have a PLQY of 1.21% corresponding to its weak blue emission. The incorporation of the inorganic structural units greatly improves the emission efficiency of the organic component, leading to 23.06% and 3.97% PLQYs for (P-xd)$ZnCl_4$ and (P-xd)$CdCl_4$, respectively. Notably, PLQY of 23.06% for (P-xd)$ZnCl_4$ is the highest reported for self-activated hybrid organic-inorganic zinc halides (see Table S6). The greater intermolecular separations of organic units in (P-xd)$ZnCl_4$ and (P-xd)$CdCl_4$ compared to the organic precursor salt results in considerable enhancement of PLQY values in hybrid materials.[24,28] The lower PLQY of (P-xd)$CdCl_4$ compared to that of (P-xd)$ZnCl_4$ can be attributed to multiple factors, such as their drastically different crystal and electronic structures (see below). The 2D-connectivity of inorganic structural units in (P-xd)$CdCl_4$ is expected to lead to more charge delocalization throughout the material, and indeed the optical absorption data suggests there may be contributions to the optical properties from both the organic and inorganic structural units. Furthermore, the PLE and PL spectra of the organic salt and (P-xd)$CdCl_4$ noticeably overlap within the 300 nm to 420 nm region, while the excitation and emission spectra of (P-xd)$ZnCl_4$ show markedly less overlap in this region (Fig. 4a – c). These results suggest negligible self-absorption in (P-xd)$ZnCl_4$ while the organic salt and (P-xd)$CdCl_4$ suffer from self-absorption of their emitted light, contributing to their reduced emission efficiency values.

Electronic band structures and density of states (DOS) were calculated for (P-xd)$ZnCl_4$ and (P-xd)$CdCl_4$, which were based on optimized structures of the experimentally determined crystal structures. Employing the many-body GW and GW-BSE methods for accurate determination of the fundamental gap and optical gap, as we previously showed for the parent 3D lead iodide perovskite,[51] is desirable, but such calculations are formidable for the HOIMs structures studied here. The fundamental bandgap is underestimated when using the PBE exchange-correlation functional, and thus could be in better agreement with the optical gap for these materials, which demonstrate relatively larger exciton binding energies due to quantum and dielectric confinement. In using the range separated hybrid functional HSE rather than PBE (see computational details in Section 2.11.), the fundamental bandgap would be calculated more accurately, and thus expected to be larger than the experimentally determined optical gap values. The band structures and projected DOS (PDOS) calculated with the HSE functional are summarized in Fig. 6. Band dispersions are stronger overall for (P-xd)$CdCl_4$ due to its higher 2D-connectivity than for the 0D-connectivity of the structural units in compound (P-xd)$ZnCl_4$. The PDOS for (P-xd)$ZnCl_4$ indicate similar energies near the valence band maximum (VBM) for the inorganic and organic components, while the electronic states from the inorganic part are further away from the conduction band minimum (CBM). In contrast, the electronic states from the inorganic component of (P-xd)$CdCl_4$ are below the states from the organic component in CBM, while the VBM has major contribution from the organic component. Detailed examinations of the PDOS are shown in Fig. S11. The individual analysis of the inorganic component indicates that the Cl *p* orbital mainly contributes to the VBM of the inorganic component in both (P-xd)$ZnCl_4$ and (P-xd)$CdCl_4$, and hybridization occurs between Zn or Cd *ns* orbitals and Cl *p* orbitals in the CBM.

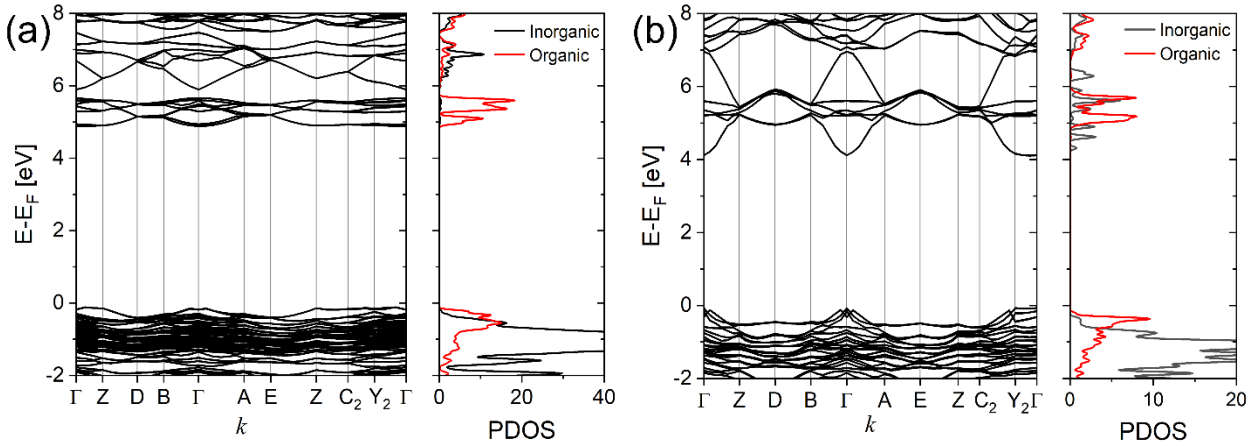

Fig. 6 HSE band structure (left panel) and PDOS (right panel) plots for (a) (P-xd)$ZnCl_4$ and (b) (P-xd)$CdCl_4$.

The VBM-CBM bandgaps for the organic cations are 5.03 and 5.05 eV for (P-xd)$ZnCl_4$ and (P-xd)$CdCl_4$, respectively, corresponding to the experimental sharp absorption peaks from the organic cation at 4.39 and 4.36 eV, respectively. A similar wide bandgap trend is predicted correctly, while the overestimation results from lack of optical gap calculation at high accuracy

for compounds with large exciton binding energies, as discussed above. Indeed, the band structures and PDOS calculated with the PBE exchange-correlation functional (summarized in Fig. S12), result in bandgap values of 3.99 and 4.03 eV for the (P-xd)$ZnCl_4$ and (P-xd)$CdCl_4$ organic components, respectively. The HSE band structure and PDOS indicate a smaller bandgap, of 4.22 eV, for the inorganic component of (P-xd)$CdCl_4$, consistent with the experimental mid-gap. The inorganic component in (P-xd)$CdCl_4$ with a 2D rather than a 0D-connectivity has weaker DOS near the CBM than the DOS from the organic cation. The experimental PL emission characteristics of (P-xd)$ZnCl_4$ and (P-xd)$CdCl_4$ can be rationalized by the results obtained from these electronic structures. According to literature studies, typically hybrid materials possessing Type-I alignment (Fig. S13a), where the VBM and CBM both consist of similar types of structural units, exhibit high emission efficiency.[24,28,34,49,52] In the case of (P-xd)$ZnCl_4$, as both the VBM and CBM are consist of the organic component, optical transitions localized on the same structural units occur, yielding considerably high PLQY. On the contrary, hybrids containing Type-II alignment (Fig. S13b), where the VBM and CBM are composed of different types of structural units, exhibit comparatively low PLQY due to the spatial separation of charge carriers and an increase in non-radiative recombination of excitons.[31,50,53] Here, in the case of Type-II alignment in (P-xd)$CdCl_4$, the high energy excitons concentrate in the organic units upon excitation at PLE_{max}. Then part of the excitons undergo quick relaxation to the lowest-lying excited states coming from the ionically bonded (unlike organometallic compounds) inorganic 2D network, where energy dissipates and facilitates the non-radiative recombination of excitons, resulting in a much lower PLQY in (P-xd)$CdCl_4$ compared to (P-xd)$ZnCl_4$. Therefore, high energy excitation of (P-xd)$CdCl_4$ probably corresponds to the emission characteristics of organic component with emission peak at around 440 nm. Similar types of emission pathways are also observed for several Cd based Type-II hybrids.[31,32,54]

In summary, the results of the thorough investigation of the optical and electronic properties of (P-xd)$ZnCl_4$ and (P-xd)$CdCl_4$ led us to attribute the blue emission of (P-xd)$ZnCl_4$ to its organic structural components. Although, both organic and inorganic units play important roles in the PL properties of the compound (P-xd)$CdCl_4$, the organic structural component is the major contributor to its blue emission at PLE_{max}. The electrons are excited from the ground state (S_0) to a high energy singlet state (S_n) upon UV excitation, and then relax to a low energy singlet state (S_1) via fast internal conversion. Finally, the radiative recombination of electrons and holes to reform the ground state produces their bright blue emission. This proposed mechanism (Fig. S14) is in excellent agreement with the reports on other hybrid materials whose PL properties are dominated by organic-based emission.[27,28,35]

3.2. Applications

The much improved air-, thermal- and photostability of (P-xd)$ZnCl_4$ and (P-xd)$CdCl_4$ allow us to make polymer-based luminescent inks to demonstrate their potential for practical applications. Bright blue luminescent inks were prepared by dispersing polycrystalline powder samples of (P-xd)$ZnCl_4$ and (P-xd)$CdCl_4$ in PMMA (see Fig. S15). Fingerprints are commonly used for control of access, national security, forensic investigations, and medical diagnosis.[55] For a reliable identification of individuals, details of different features of latent fingerprints (LFP) are required.[56,57] For this application, (P-xd)$ZnCl_4$ has several added advantages including its high-efficiency PL and earth-abundant and non-toxic elemental composition.[58] Fig. 7 shows a luminescent fingerprint using the (P-xd)$ZnCl_4$ ink on a glass surface. The magnified images of

the LFP patterns under UV irradiation clearly show the latent features of the fingerprint such as pore, island, hook, termination, etc., that are essential for distinguishing individuals. Naked eye visualization of these features indicates the strong potential of (P-xd)$ZnCl_4$ for this application. Furthermore, the luminescent inks based on (P-xd)$ZnCl_4$ and (P-xd)$CdCl_4$ can also be used for anti-counterfeiting. To demonstrate this, graffiti of the word "OU" was drawn on black paper. In both cases, clearly discernible differences of the graffiti are observed under UV irradiation (Fig. 8a and b), which indicates the suitability of (P-xd)$ZnCl_4$ and (P-xd)$CdCl_4$ for use as anti-counterfeiting tags. Yet another potential application of emissive metal halides is their use as phosphors in solid-state lighting and displays.[59,60] For these applications, the inexpensive preparation, earth-abundant elemental compositions, and broadband emission characteristics of (P-xd)$ZnCl_4$ and (P-xd)$CdCl_4$ are attractive. As a proof of concept, UV-pumped white LEDs were fabricated by coating the luminescent inks of (P-xd)$ZnCl_4$ and (P-xd)$CdCl_4$ onto commercial 365 nm LEDs. The fabricated LEDs show bright distinguishable bluish-white luminescence (Fig. 8), and the features of the PL spectra of (P-xd)$ZnCl_4$ and (P-xd)$CdCl_4$ are observed in the corresponding UV-pumped EL spectra. Further optimization of the material chemistries and structures could provide a route for preparation of single component white light emitting hybrid group 12 metal halides.

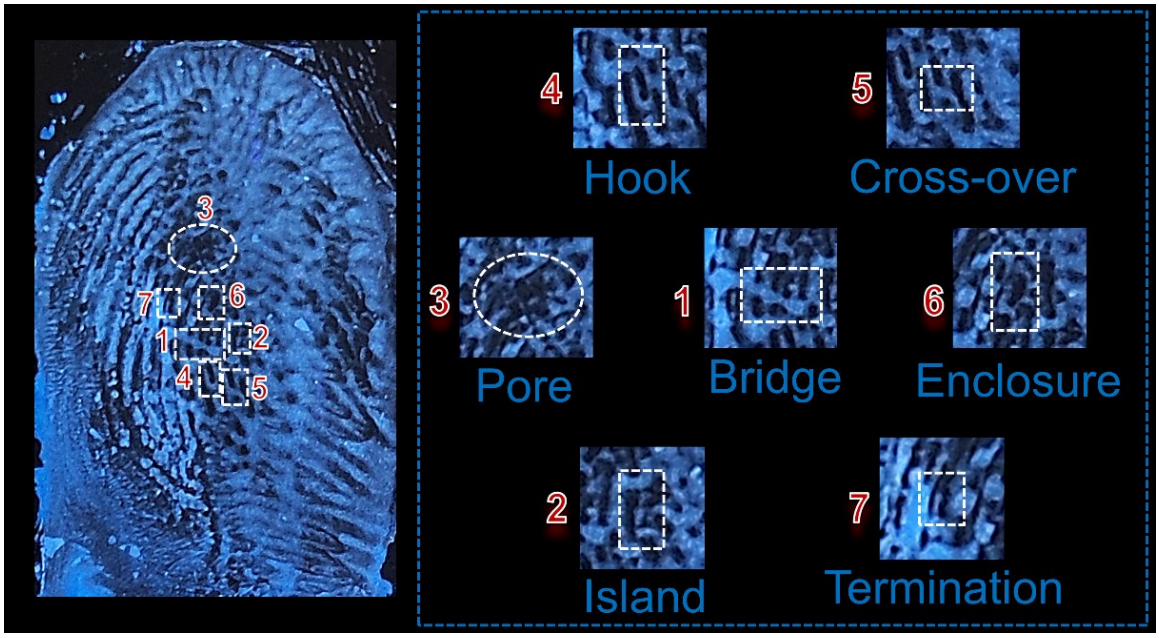

Fig. 7 Ultra-bright blue luminescent latent fingerprints (LFP) based on a (P-xd)$ZnCl_4$ ink visualized under UV irradiation. The magnified images represent the specific details: (1) bridge, (2) island, (3) pore, (4) hook, (5) cross-over, (6) enclosure, and (7) termination.

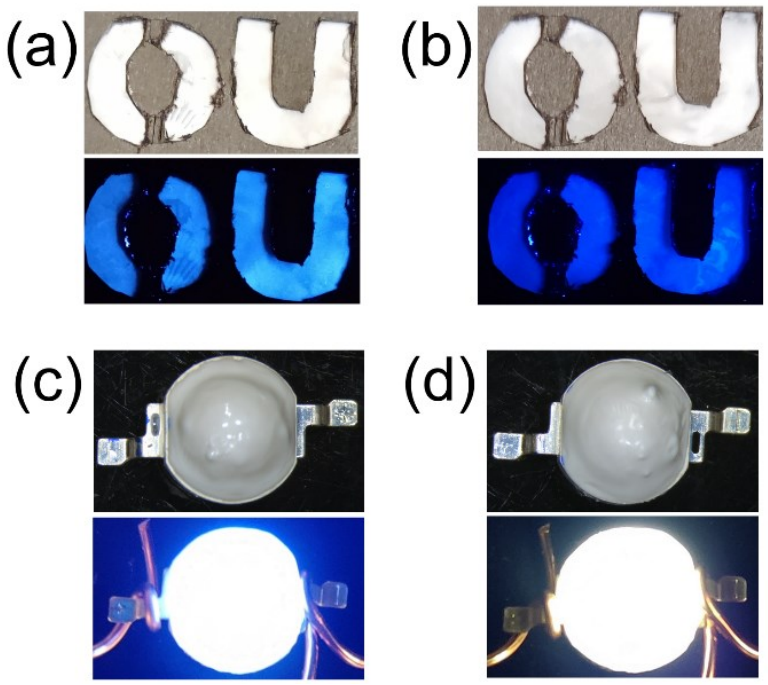

Fig. 8 Photographs of 'OU' graffiti prepared using luminescent inks of (a) (P-xd)$ZnCl_4$ and (b) (P-xd)$CdCl_4$ (top: under ambient light; bottom: under 245 nm UV light). (c-d) Photographs of white LEDs fabricated by coating commercial 365 UV LEDs with (P-xd)$ZnCl_4$ and (P-xd)$CdCl_4$, respectively (top: light-off state; bottom: light-on state).

4. Conclusion

In summary, this work reports synthesis, structural, optical, and electronic characterizations of two novel compounds, (P-xd)$ZnCl_4$ and (P-xd)$CdCl_4$. (P-xd)$ZnCl_4$ possesses a crystal structure with completely isolated $[ZnCl_4]^{2-}$ tetrahedral units with 0D-connectivity in a pseudo-layered organic $(P\text{-xd})^{2+}$ matrix. In contrast, (P-xd)$CdCl_4$ adopts a 2D layered perovskite structure containing corner-sharing $[CdCl_6]^{4-}$ octahedral units with alternating layers of organic cations. The hybrid compounds (P-xd)$ZnCl_4$ and (P-xd)$CdCl_4$ are found to demonstrate improved ambient air-, thermal- and photo-stability. Our structural, experimental, and computational studies show that the emission of (P-xd)$ZnCl_4$ originates from its organic component $(P\text{-xd})^{2+}$ with nearly 23 times increased PLQY than that of the organic precursor. In contrast, (P-xd)$CdCl_4$ exhibits nearly 4 times higher PLQY than the organic precursor, but its PLQY is markedly lower than that of (P-xd)$ZnCl_4$. This has been attributed to its different electronic structure; the top of the VB and bottom of the CB are dominated by contributions from the organic and inorganic structural components, respectively, yielding a Type-II band alignment for (P-xd)$CdCl_4$. Notably, the PLQY of 23% for (P-xd)$ZnCl_4$ is the highest reported to date for Zn-based HOIMs where the emission originates from the organic component. This remarkable increase in the PLQY of (P-xd)$ZnCl_4$ is attributed to its unique crystal and electronic structure – (P-xd)$ZnCl_4$ shows a Type-I band alignment with higher charge localization in its structural units of 0D-connectivity. The highly ordered structure of (P-xd)$ZnCl_4$ features strong H-bonding interactions and intermolecular arrangements that reduce the concentration quenching of excitons within the organic molecules. The results of this work suggest that the emission efficiency of the

organic components can be much improved in a hybrid metal halide lattice while largely preserving the original photoluminescence peak and shape. Further structural and chemical composition optimizations may lead to even higher organic emission efficiencies when paired with group 12 metal halides. Ultimately, the incorporation of affordable and earth-abundant group 12 metals into hybrid halides may pave the way for their practical use in optical applications.

Author Contributions

D. A. Popy: carried out synthesis, optical characterization, and application experiments, analyzed results, and wrote the manuscript. B. N. Evans: carried out synthesis, optical characterization and analyzed results. T. D. Creason: analyzed data. D. Banerjee: analyzed optical application data. D. T. Glatzhofer: prepared the organic salt and hybrids. J. Jiang and R. Pachter: carried out the theoretical calculations and wrote the corresponding part of the manuscript. L. M. Loftus: measured PL lifetimes and analyzed corresponding results. B. Saparov conceived and supervised the work and wrote the manuscript. All authors have approved the final version of the manuscript.

Declaration of competing interest

The authors declare that they have no known competing financial interests or personal relationships that could have appeared to influence the work reported in this paper.

Acknowledgement

This work was supported by the National Science Foundation (NSF DMR-2045490). We thank Dr. Douglas Powel for the help with SCXRD measurements (supported by NSF grant CHE-1726630).

Appendix A. Supplementary data

Electronic supplementary information (ESI) available: Single crystal X-ray diffraction data and refinement parameters, crystal images, PXRD, air and moisture stability test results, CIE plots, PL lifetimes and the DFT data. For ESI and crystallographic data in CIF or other electronic format see DOI.

Data availability

The raw/processed data required to reproduce these findings cannot be shared at this time due to technical or time limitations.

References

1. Zou, S.-J., Shen, Y., Xie, F.-M., Chen, J.-D., Li, Y.-Q., Tang, J.-X., Recent Advances in Organic Light-emitting Diodes: Toward Smart Lighting and Displays, Mater. Chem. Front. 4 (3) (2020) 788-820, 10.1039/C9QM00716D.
2. Zhao, G., Dong, H., Liao, Q., Jiang, J., Luo, Y., Fu, H., Hu, W., Organic Field-effect Optical Waveguides, Nat. Commun. 9 (1) (2018) 4790, 10.1038/s41467-018-07269-9.
3. Zang, L., Che, Y., Moore, J. S., One-Dimensional Self-Assembly of Planar π-Conjugated Molecules: Adaptable Building Blocks for Organic Nanodevices, Acc. Chem. Res. 41 (12) (2008) 1596-1608, 10.1021/ar800030w.
4. Yao, X., Li, T., Wang, J., Ma, X., Tian, H., Recent Progress in Photoswitchable Supramolecular Self-Assembling Systems, Adv. Opt. Mater. 4 (9) (2016) 1322-1349, https://doi.org/10.1002/adom.201600281.
5. Shoji, Y., Ikabata, Y., Wang, Q., Nemoto, D., Sakamoto, A., Tanaka, N., Seino, J., Nakai, H., Fukushima, T., Unveiling a New Aspect of Simple Arylboronic Esters: Long-Lived Room-Temperature Phosphorescence from Heavy-Atom-Free Molecules, J. Am. Chem. Soc 139 (7) (2017) 2728-2733, 10.1021/jacs.6b11984.
6. Hirata, S., Totani, K., Zhang, J., Yamashita, T., Kaji, H., Marder, S. R., Watanabe, T., Adachi, C., Efficient Persistent Room Temperature Phosphorescence in Organic Amorphous Materials under Ambient Conditions, Adv. Funct. Mater. 23 (27) (2013) 3386-3397, https://doi.org/10.1002/adfm.201203706.
7. Benson, C. R., Kacenauskaite, L., VanDenburgh, K. L., Zhao, W., Qiao, B., Sadhukhan, T., Pink, M., Chen, J., Borgi, S., Chen, C.-H., Davis, B. J., Simon, Y. C., Raghavachari, K., Laursen, B. W., Flood, A. H., Plug-and-Play Optical Materials from Fluorescent Dyes and Macrocycles, Chem 6 (8) (2020) 1978-1997, 10.1016/j.chempr.2020.06.029.
8. Guo, Y., Xu, L., Liu, H., Li, Y., Che, C.-M., Li, Y., Self-Assembly of Functional Molecules into 1D Crystalline Nanostructures, Adv. Mater. 27 (6) (2015) 985-1013, https://doi.org/10.1002/adma.201403846.
9. Desiraju, G., Crystal Engineering. From Molecules to Crystals, Acta Cryst. A 67 (a1) (2011) C18-C19, doi:10.1107/S0108767311099600.
10. Wang, C., and Li, Z., Molecular Conformation and Packing: their Critical Roles in the Emission Performance of Mechanochromic Fluorescence Materials, Mater. Chem. Front. 1 (11) (2017) 2174-2194, 10.1039/C7QM00201G.
11. Asad, M., Wang, Y.-J., Wang, S., Dong, Q.-G., Li, L.-K., Majeed, S., Wang, Q.-Y., Zang, S.-Q., Hydrazone Connected Stable Luminescent Covalent–organic Polymer for Ultrafast Detection of Nitro-explosives, RSC Adv. 11 (62) (2021) 39270-39277, 10.1039/D1RA08009A.
12. Dang, D., Wang, X., Wang, D., Yang, Z., Hao, D., Xu, Y., Zhang, S., Meng, L., Fluorescent Organic Nanoparticles Constructed by a Facile "Self-Isolation Enhanced Emission" Strategy for Cell Imaging, ACs Appl. Nano Mater. 1 (5) (2018) 2324-2331, 10.1021/acsanm.8b00409.
13. Xiao, G., Ma, Y.-J., Fang, X., Yan, D., Quadruple Anticounterfeiting Encryption: Anion-Modulated Forward and Reverse Excitation-Dependent Multicolor Afterglow in Two-Component Ionic Crystals, ACS Appl. Mater. Interfaces 14 (26) (2022) 30246-30255, 10.1021/acsami.2c08379.

14. Al-Attar, H. A., and Monkman, A. P., Room-Temperature Phosphorescence From Films of Isolated Water-Soluble Conjugated Polymers in Hydrogen-Bonded Matrices, Adv. Funct. Mater. 22 (18) (2012) 3824-3832, https://doi.org/10.1002/adfm.201200814.
15. Yu, Y., Kwon, M. S., Jung, J., Zeng, Y., Kim, M., Chung, K., Gierschner, J., Youk, J. H., Borisov, S. M., Kim, J., Room-Temperature-Phosphorescence-Based Dissolved Oxygen Detection by Core-Shell Polymer Nanoparticles Containing Metal-Free Organic Phosphors, Angew. Chem. Int. Ed. 56 (51) (2017) 16207-16211, https://doi.org/10.1002/anie.201708606.
16. Saparov, B., and Mitzi, D. B., Organic–Inorganic Perovskites: Structural Versatility for Functional Materials Design, Chem. Rev. 116 (7) (2016) 4558-4596, 10.1021/acs.chemrev.5b00715.
17. Manser, J. S., Christians, J. A., Kamat, P. V., Intriguing Optoelectronic Properties of Metal Halide Perovskites, Chem. Rev. 116 (21) (2016) 12956-13008, 10.1021/acs.chemrev.6b00136.
18. Mitzi, D. B., Templating and Structural Engineering in Organic–inorganic Perovskites, J. Chem. Soc., Dalton Trans. (1) (2001) 1-12, 10.1039/B007070J.
19. Deschler, F., Price, M., Pathak, S., Klintberg, L. E., Jarausch, D.-D., Higler, R., Hüttner, S., Leijtens, T., Stranks, S. D., Snaith, H. J., Atatüre, M., Phillips, R. T., Friend, R. H., High Photoluminescence Efficiency and Optically Pumped Lasing in Solution-Processed Mixed Halide Perovskite Semiconductors, J. Phys. Chem. Lett. 5 (8) (2014) 1421-1426, 10.1021/jz5005285.
20. Li, X., Gao, X., Zhang, X., Shen, X., Lu, M., Wu, J., Shi, Z., Colvin, V. L., Hu, J., Bai, X., Yu, W. W., Zhang, Y., Lead-Free Halide Perovskites for Light Emission: Recent Advances and Perspectives, Adv. Sci. 8 (4) (2021) 2003334, https://doi.org/10.1002/advs.202003334.
21. Roccanova, R., Ming, W., Whiteside, V. R., McGuire, M. A., Sellers, I. R., Du, M.-H., Saparov, B., Synthesis, Crystal and Electronic Structures, and Optical Properties of $(CH_3NH_3)_2CdX_4$ (X = Cl, Br, I), Inorg. Chem. 56 (22) (2017) 13878-13888, 10.1021/acs.inorgchem.7b01986.
22. Yangui, A., Roccanova, R., McWhorter, T. M., Wu, Y., Du, M.-H., Saparov, B., Hybrid Organic–Inorganic Halides $(C_5H_7N_2)_2MBr_4$ (M = Hg, Zn) with High Color Rendering Index and High-Efficiency White-Light Emission, Chem. Mater. 31 (8) (2019) 2983-2991, 10.1021/acs.chemmater.9b00537.
23. Yangui, A., Roccanova, R., Wu, Y., Du, M.-H., Saparov, B., Highly Efficient Broad-Band Luminescence Involving Organic and Inorganic Molecules in a Zero-Dimensional Hybrid Lead Chloride, J. Phys. Chem. C 123 (36) (2019) 22470-22477, 10.1021/acs.jpcc.9b05509.
24. Zhou, C., Worku, M., Neu, J., Lin, H., Tian, Y., Lee, S., Zhou, Y., Han, D., Chen, S., Hao, A., Djurovich, P. I., Siegrist, T., Du, M.-H., Ma, B., Facile Preparation of Light Emitting Organic Metal Halide Crystals with Near-Unity Quantum Efficiency, Chem. Mater. 30 (7) (2018) 2374-2378, 10.1021/acs.chemmater.8b00129.
25. Song, G., Li, Z., Gong, P., Xie, R.-J., Lin, Z., Tunable White Light Emission in a Zero-Dimensional Organic–Inorganic Metal Halide Hybrid with Ultra-High Color Rendering Index, Adv. Opt. Mater. 9 (11) (2021) 2002246, https://doi.org/10.1002/adom.202002246.
26. Chaaban, M., Ben-Akacha, A., Worku, M., Lee, S., Neu, J., Lin, X., Vellore Winfred, J. S. R., Delzer, C. J., Hayward, J. P., Du, M.-H., Siegrist, T., Ma, B., Metal Halide Scaffolded Assemblies of Organic Molecules with Enhanced Emission and Room Temperature

Phosphorescence, J. Phys. Chem. Lett. 12 (34) (2021) 8229-8236, 10.1021/acs.jpclett.1c02354.
27. Su, B., Song, G., Molokeev, M. S., Golovnev, N. N., Lesnikov, M. K., Lin, Z., Xia, Z., Role of Metal–Chloride Anions in Photoluminescence Regulations for Hybrid Metal Halides, J. Phys. Chem. Lett. 12 (7) (2021) 1918-1925, 10.1021/acs.jpclett.1c00182.
28. Zhou, S., Zhou, L., Chen, Y., Shen, W., Li, M., He, R., Boosting Blue Emission of Organic Cations in a Sn(IV)-Based Perovskite by Constructing Intermolecular Interactions, J. Phys. Chem. Lett. 13 (37) (2022) 8717-8724, 10.1021/acs.jpclett.2c02413.
29. Allred, A. L., Electronegativity Values from Thermochemical Data, J. Inorg. Nucl. Chem. 17 (3) (1961) 215-221, https://doi.org/10.1016/0022-1902(61)80142-5.
30. McWhorter, T. M., Zhang, Z., Creason, T. D., Thomas, L., Du, M. H., Saparov, B., $(C_7H_{11}N_2)_2MBr_4$ (M=Cu, Zn): X‐Ray Sensitive 0D Hybrid Metal Halides with Tunable Broadband Emission, Eur. J. Inorg. Chem. 2022 (10) (2022) e202100954, 10.1002/ejic.202100954.
31. Roccanova, R., Houck, M., Yangui, A., Han, D., Shi, H., Wu, Y., Glatzhofer, D. T., Powell, D. R., Chen, S., Fourati, H., Lusson, A., Boukheddaden, K., Du, M. H., Saparov, B., Broadband Emission in Hybrid Organic-Inorganic Halides of Group 12 Metals, ACS Omega 3 (12) (2018) 18791-18802, 10.1021/acsomega.8b02883.
32. Yangui, A., Pillet, S., Bendeif, E.-E., Lusson, A., Triki, S., Abid, Y., Boukheddaden, K., Broadband Emission in a New Two-Dimensional Cd-Based Hybrid Perovskite, ACS Photonics 5 (4) (2018) 1599-1611, 10.1021/acsphotonics.8b00052.
33. Zhang, X., Xiong, Y., Liu, K., Wang, N., Fan, L., Li, W., Zhao, X., Zhao, J., Liu, Q., Thermal Stable Zinc-based Hybrid Halides with High External Quantum Efficiency as Temperature Detectors, J. Mater. Chem. C 10 (36) (2022) 13137-13142, 10.1039/D2TC02838G.
34. Ma, Y. Y., Sun, Y. M., Xu, W. J., Liu, X. L., Zhong, Q. Q., Song, Y. R., Fu, H. Q., Yue, C. Y., Lei, X. W., Ultrastable 0D Organic Zinc Halides with Highly Efficient Blue Light Emissions, Adv. Opt. Mater. 10 (17) (2022) 2200386, 10.1002/adom.202200386.
35. Li, K.-J., Zhao, Y.-Y., Sun, M.-E., Chen, G.-S., Zhang, C., Liu, H.-L., Li, H.-Y., Zang, S.-Q., Mak, T. C. W., Zero-Dimensional Zinc Halide Organic Hybrids with Excellent Optical Waveguide Properties, Cryst. Growth Des. 22 (5) (2022) 3295-3302, 10.1021/acs.cgd.2c00117.
36. Arkenbout, A. H., Meetsma, A., Palstra, T. T. M., (*p*-Phenylenedimethylene)diammonium dichloride, Acta Cryst. E 63 (2) (2007) o869-o870, 10.1107/s1600536807002619.
37. Kresse, G., and Furthmüller, J., Efficiency of ab-Initio Total Energy Calculations for Metals and Semiconductors Using a Plane-Wave Basis Set, Comput. Mater. Sci. 6 (1) (1996) 15-50, https://doi.org/10.1016/0927-0256(96)00008-0.
38. Kresse, G., and Joubert, D., From Ultrasoft Pseudopotentials to the Projector Augmented-Wave Method, Phys. Rev. B 59 (3) (1999) 1758-1775, 10.1103/PhysRevB.59.1758.
39. Perdew, J. P., Burke, K., Ernzerhof, M., Generalized Gradient Approximation Made Simple, Phys. Rev. Lett. 78 (7) (1997) 1396-1396, 10.1103/PhysRevLett.78.1396.
40. Grimme, S., Antony, J., Ehrlich, S., Krieg, H., A Consistent and Accurate ab Initio Parametrization of Density Functional Dispersion Correction (DFT-D) for the 94 Elements H-Pu, J. Chem. Phys. 132 (15) (2010) 154104, 10.1063/1.3382344.

41. Beck, H., Gehrmann, C., Egger, D. A., Structure and Binding in Halide Perovskites: Analysis of Static and Dynamic Effects from Dispersion-corrected Density Functional Theory, APL Mater. 7 (2) (2019) 021108, 10.1063/1.5086541.
42. Zhang, L., and Liang, W., How the Structures and Properties of Two-Dimensional Layered Perovskites $MAPbI_3$ and $CsPbI_3$ Vary with the Number of Layers, J. Phys. Chem. Lett. 8 (7) (2017) 1517-1523, 10.1021/acs.jpclett.6b03005.
43. Heyd, J., Scuseria, G. E., Ernzerhof, M., Hybrid Functionals Based on a Screened Coulomb Potential, J. Chem. Phys. 118 (18) (2003) 8207-8215, 10.1063/1.1564060.
44. Krukau, A. V., Vydrov, O. A., Izmaylov, A. F., Scuseria, G. E., Influence of the Exchange Screening Parameter on the Performance of Screened Hybrid Functionals, J. Chem. Phys. 125 (22) (2006) 224106, 10.1063/1.2404663.
45. Shannon, R. D., Revised Effective Ionic Radii and Systematic Studies of Interatomic Distances in Halides and Chalcogenides, Acta Cryst. A 32 (5) (1976) 751-767, 10.1107/s0567739476001551.
46. Alvarez, S., A Cartography of the Van der Waals Territories, Dalton Trans. 42 (24) (2013) 8617-8636, 10.1039/C3DT50599E.
47. Jeffrey, G. A., *An Introduction to Hydrogen Bonding*. Oxford university press New York: 1997
48. Gautier, R., Paris, M., Massuyeau, F., Hydrogen Bonding and Broad-Band Emission in Hybrid Zinc Halide Phosphors, Inorg. Chem. 59 (5) (2020) 2626-2630, 10.1021/acs.inorgchem.9b02964.
49. Creason, T. D., Fattal, H., Gilley, I. W., Evans, B. N., Jiang, J., Pachter, R., Glatzhofer, D. T., Saparov, B., Stabilized Photoemission from Organic Molecules in Zero-dimensional Hybrid Zn and Cd Halides, Inorg. Chem. Front. (2022) 10.1039/D2QI01293F.
50. Popy, D. A., Creason, T. D., Zhang, Z., Singh, D. J., Saparov, B., Electronic Structures and Optical Properties of $(Ph_4P)MX_2$ (M = Cu, Ag; X = Cl, Br), J. Solid State Chem. 316 (2022) 123626, https://doi.org/10.1016/j.jssc.2022.123626.
51. Jiang, J., Pachter, R., Yang, Y., Bellaiche, L., Dependence of the Electronic and Optical Properties of Methylammonium Lead Triiodide on Ferroelectric Polarization Directions and Domains: A First Principles Computational Study, J. Phys. Chem. C 121 (28) (2017) 15375-15383, 10.1021/acs.jpcc.7b04557.
52. Fang, Y., Liu, W., Teat, S. J., Dey, G., Shen, Z., An, L., Yu, D., Wang, L., O'Carroll, D. M., Li, J., A Systematic Approach to Achieving High Performance Hybrid Lighting Phosphors with Excellent Thermal- and Photostability, Adv. Funct. Mater. 27 (3) (2017) 1603444, https://doi.org/10.1002/adfm.201603444.
53. Qi, Z., Gao, H., Zhu, X., Lu, Z., Zhang, X.-M., Blue Light-Excitable Broadband Yellow Emission in a Zero-Dimensional Hybrid Bismuth Halide with Type-II Band Alignment, Inorg. Chem. 61 (48) (2022) 19483-19491, 10.1021/acs.inorgchem.2c03409.
54. Yuan, J.-T., Zhou, G., Zhang, J., Zhang, X.-M., Synergetic Model for Implementing Single-Component White-Light Emission: A Case Study of Zero-Dimensional Cadmium Halides, Mater. Chem. Front. (2023) 10.1039/D2QM01049F.
55. Bramble, S. K., Creer, K. E., Gui Qiang, W., Sheard, B., Ultraviolet Luminescence from Latent Fingerprints, Forensic Sci. Int. 59 (1) (1993) 3-14, https://doi.org/10.1016/0379-0738(93)90306-U.

56. Wang, C.-F., Cheng, R., Ji, W.-Q., Ma, K., Ling, L., Chen, S., Recognition of Latent Fingerprints and Ink-Free Printing Derived from Interfacial Segregation of Carbon Dots, ACS Appl. Mater. Interfaces 10 (45) (2018) 39205-39213, 10.1021/acsami.8b13545.
57. Chen, H., Chang, K., Men, X., Sun, K., Fang, X., Ma, C., Zhao, Y., Yin, S., Qin, W., Wu, C., Covalent Patterning and Rapid Visualization of Latent Fingerprints with Photo-Cross-Linkable Semiconductor Polymer Dots, ACS Appl. Mater. Interfaces 7 (26) (2015) 14477-14484, 10.1021/acsami.5b03749.
58. Roohani, N., Hurrell, R., Kelishadi, R., Schulin, R., Zinc and its Importance for Human Health: An Integrative Review, J. Res. Med. Sci. 18 (2) (2013) 144,
59. Kimura-Minoda, T., and Ayama, M., Evaluation of Discomfort Glare from Color Leds and its Correlation with Individual Variations in Brightness Sensitivity, Color Res. Appl. 36 (4) (2011) 286-294, https://doi.org/10.1002/col.20630.
60. Steigerwald, D. A., Bhat, J. C., Collins, D., Fletcher, R. M., Holcomb, M. O., Ludowise, M. J., Martin, P. S., Rudaz, S. L., Illumination with Solid State Lighting Technology, IEEE J. Sel. Topics Quantum Electron. 8 (2) (2002) 310-320, 10.1109/2944.999186.

Table of Content

The highly ordered intermolecular rearrangement due to the incorporation of group 12 metal (Zn and Cd) halides in *p*-xylylenediammonium resulted nearly 23 and 4 times higher emission efficiency in hybrid (P-xd)$ZnCl_4$ and (P-xd)$CdCl_4$ than that of the organic component.